Metals and Materials International (2019) 25:140–146
https://doi.org/10.1007/s12540-018-0176-6

Microstructural Evolution of Oxide and Nitride Dispersed Nickel-Based Alloy Powders

Man Wang[1,2] · Heung Nam Han[2] · Hee-Suk Chung[3] · Young-Bum Chun[1] · Jinsung Jang[1]

Received: 5 April 2018 / Accepted: 5 August 2018 / Published online: 14 August 2018
© The Korean Institute of Metals and Materials 2018

Abstract
The microstructural evolution of oxide and nitride dispersed nickel-based mechanical alloyed (MA) powders was investigated using in situ characterization methods, including high-temperature X-ray diffraction and transmission electron microscope (TEM). MA powders strengthened by Si_3N_4 and Er_2O_3 exhibited different behaviors. The added Si_3N_4 particles were not dissolved during the MA process, resulting in faster strain recovery and grain coarsening in the MA powders. In contrast, the Er_2O_3 particles were dissolved into the matrix during the MA process. Also, precipitation of $Er_2Ti_2O_7$ particles with an average size of 10 nm was observed by in situ TEM. The precipitation of nanoparticles was related to strain recovery and grain growth, as both reduced the solubility of solute atoms in the matrix. The in situ TEM observation results provide direct experimental evidence for the dissolution–precipitation mechanism in nickel-based MA powders.

Keywords Nickel alloy · Oxide dispersion strengthening · Mechanical alloying · In situ TEM · Precipitation

1 Introduction

Oxide dispersion strengthened (ODS) alloys are important candidate materials for advanced nuclear reactors because of their excellent creep properties and irradiation resistance [1–3]. These properties are ascribed to the dispersion of nanoparticles in the matrix, which can serve as dislocation obstacles and sinks for irradiation-induced defects. Therefore, understanding the formation behaviors of nanoparticles is crucial for optimizing the properties of ODS alloys.

ODS alloys are usually fabricated by mechanical alloying (MA) of oxides and pre-alloyed powders, followed by hot isostatic pressing or hot extrusion [4]. Numerous studies have focused on the formation behaviors of nanoparticles during fabrication [5–10]. The commonly proposed formation mechanism is that oxides dissolve into the matrix during MA process, and nanoparticles precipitate during consolidation. However, most previous studies have merely characterized the final materials, where information on the early stage of precipitation is very limited. On the other hand, in situ neutron techniques are valuable for studying precipitation behaviors at an early stage. Zhang et al. [7] studied the nanoparticle formation behaviors using in situ neutron diffraction in milled powders composed of Fe–14Cr–10Y_2O_3, and He et al. [11] reported that nanoparticles were observed in Fe–9Cr-based MA powders after annealing at 600 °C using in situ small-angle neutron scattering (SANS). However, neutron techniques are limited as they do not provide detailed crystal structure and morphology information of the precipitates [12].

Transmission electron microscope (TEM) is a powerful tool for investigating precipitates by providing chemical composition and crystal structure information at the same time. Furthermore, in situ TEM makes it possible to track the microstructural evolution that lead to precipitation. Therefore, in order to get a better understanding of nanoparticle formation behaviors, the microstructural evolution of oxide and nitride strengthened nickel-based MA powders was investigated using in situ TEM in this study.

✉ Jinsung Jang
jjang@kaeri.re.kr

[1] Advanced Materials Development Team, Korea Atomic Energy Research Institute, Daejeon 34057, Republic of Korea

[2] Department of Materials Science and Engineering and Research Institute of Advanced Materials, Seoul National University, Seoul 08826, Republic of Korea

[3] Jeonju Center, Korea Basic Science Institute, Jeonju 54907, Republic of Korea

Table 1 Nominal compositions of nickel-based MA powders (wt%)

	Pre-alloyed 690	Ti	Er_2O_3	Si_3N_4	Remark
1-Er_2O_3	Bal.	0.5	1.6	–	Oxide
2-Si_3N_4	Bal.	–	–	0.6	Nitride

2 Experimental Procedures

Pre-alloyed 690 powders (Ni–31Cr–11Fe, wt%) with a size of about 45 μm were used as the base material. In order to investigate the precipitation behaviors of oxide and nitride, Er_2O_3 (8–31 nm) and Si_3N_4 (15–65 nm) powders were respectively blended with the pre-alloyed 690 powders. It is well known that Ti is necessary in refinement of oxide particles [12, 13], therefore Ti powders (45 μm) were added together with Er_2O_3 powders. The nominal compositions of MA powders are listed in Table 1. The added 1.6 wt% Er_2O_3 and 0.6 wt% Si_3N_4 corresponded to the same volume fraction of 1.5%. The MA process was performed using a horizontal ball mill (Zoz Simoloyer CM08™) for 40 h at 200 rpm with a ball-to-powder ratio of 10:1 under an argon atmosphere.

High-temperature X-ray diffraction (XRD) analysis was performed using a PANalytical Empyrean diffractometer (Cu Kα radiation, λ = 1.54056 Å) with a step size of 0.0131°. XRD measurements were carried out at room temperature (RT), and then at high temperatures between 500 and 1000 °C in vacuum (10^{-4}–10^{-3} Pa). Rietveld analysis was performed on the XRD patterns using FullProf software, where the peak broadening was estimated using a pseudo-Voigt function, and the crystallite size and strain were obtained [14, 15].

Microstructural evolution was investigated using in situ TEM (JEM-ARM 200F) equipped with an in situ sample holder (Aduro 500). The TEM specimens were prepared from MA powders using a dual focused ion beam (FIB, Nova 200). The microstructural evolution of one selected area was recorded in real-time during heating. Once significant microstructural changes had occurred, the heating process was stopped, and the specimen was cooled to RT for detailed examination. The heating and cooling rates were both 1 °C s^{-1}.

3 Results and Discussion

Figure 1 shows the evolution of crystallite size and strain of nickel-based MA powders using high-temperature XRD. In the as-MA powders, both specimens had nano-sized crystallites (smaller than 15 nm) and relatively large

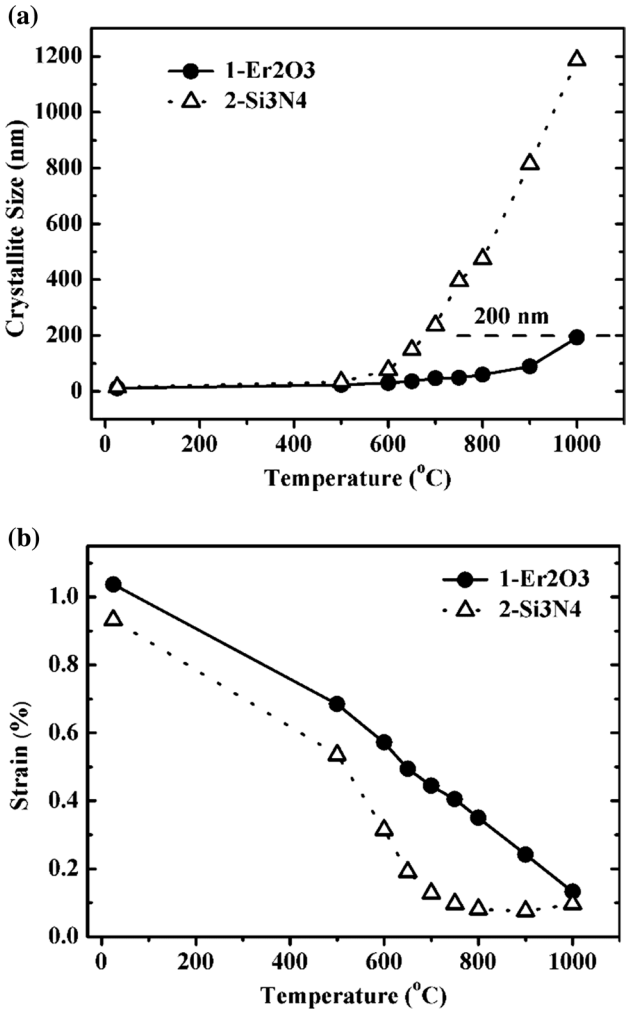

Fig. 1 Evolution of **a** crystallite size and **b** strain of nickel-based MA powders

strain. These are typical features of MA powders, as they suffer repeated welding, fracturing, and rewelding during MA process [4, 16]. However, the two MA powders exhibited different behaviors with increasing temperature. In the MA powders with addition of Er_2O_3, the crystallite size was stable, and maintained approximately 60 nm until 800 °C. As the temperature increased further, the crystallite size gradually increased. It should be noted that the crystallite size was still around 200 nm at 1000 °C. In contrast, in the MA powders with addition of Si_3N_4, the crystallite size increased significantly at temperatures above 600 °C, and the strain was quickly relieved. The different behaviors of the two MA powders are related to their microstructures.

Figure 2a is a bright field (BF) image of the as-MA powders with addition of Si_3N_4. Many white-contrast particles with sizes of 42 ± 18 nm were distributed in the as-MA powders, as indicated by the arrows in Fig. 2a. Figure 2b

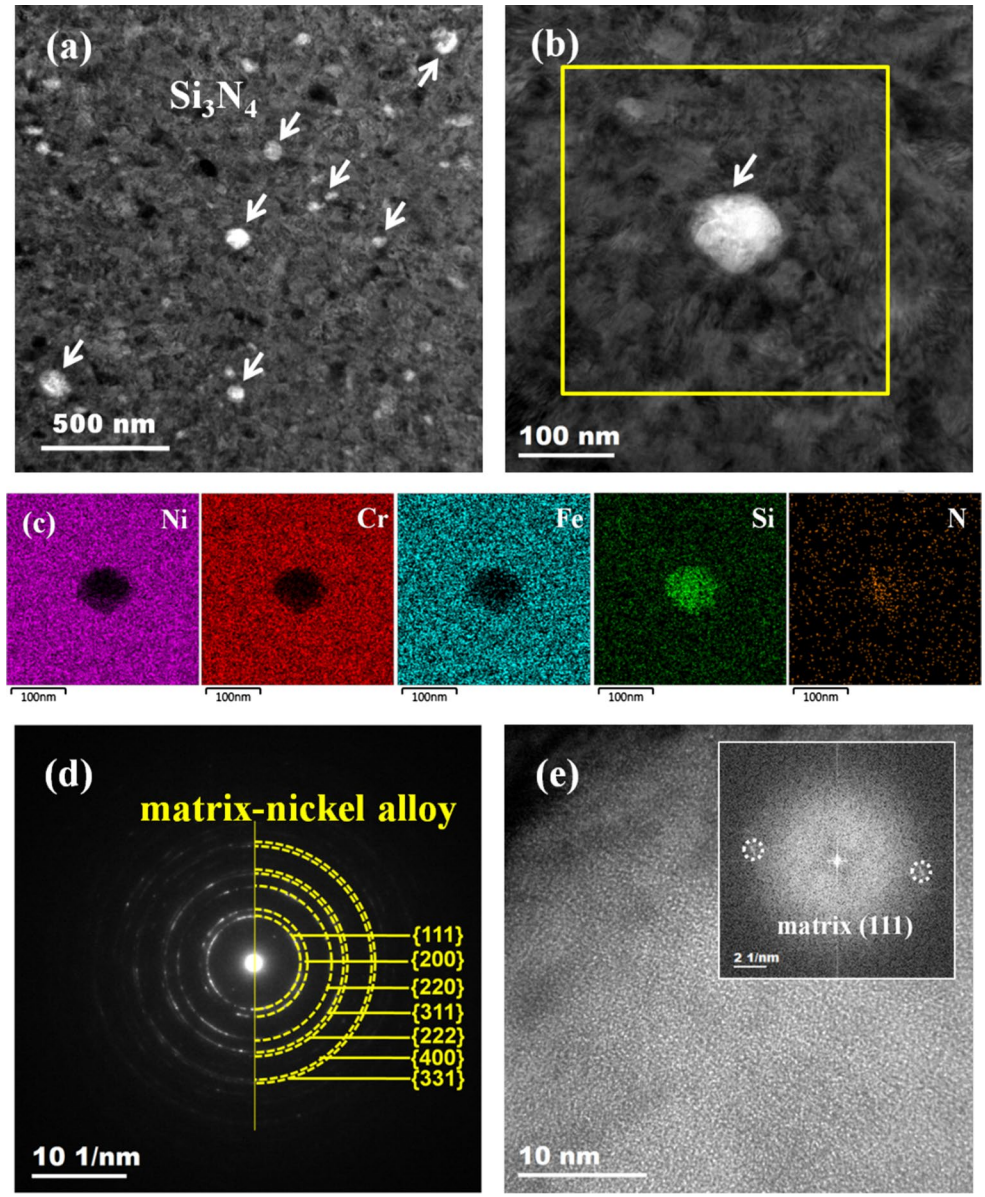

Fig. 2 TEM results of as-MA powders with addition of Si_3N_4: **a** BF-TEM image, **b** BF-TEM image of in situ observing area, **c** EDS mapping results of the squared area in (**b**), **d** SADP corresponding to (**b**), **d** HR image of the particle indicated by the arrow in (**b**) with the FFT image inset

is a BF image of the selected area for in situ observation. According to the EDS mapping results shown in Fig. 2c, the matrix was rich in Ni, Cr, and Fe, while the particle was rich in Si and N. Figure 2d is the corresponding selected area electron diffraction pattern (SADP) of Fig. 2b, which was identified to be nickel alloy phase. Figure 2e is a high resolution (HR) image of the particle. Although there were two faint diffraction spots from the matrix, there were no lattice fringes from the particle. Based on the EDS and HR analyses, this white-contrast particle was characterized to be the original amorphous Si_3N_4. It could be concluded that the added Si_3N_4 particles were not dissolved into the matrix during MA process. The possible reason for the non-dissolved Si_3N_4 may be due to its stable covalent structure. However, no particles were found in the as-MA powders with addition of Er_2O_3 (Fig. 4a), indicating that they were dissolved into the matrix during MA process.

Figure 3 shows microstructural evolution of the MA powders with addition of Si_3N_4 during heating and cooling. Recrystallization seemed to begin at around 600 °C, and grain coarsening occurred during further heating to 750 °C. Then, the heating process was stopped, and the specimen was cooled to RT. Figure 3d is a BF image showing the grain morphology, with grain size between 150 and 200 nm. The

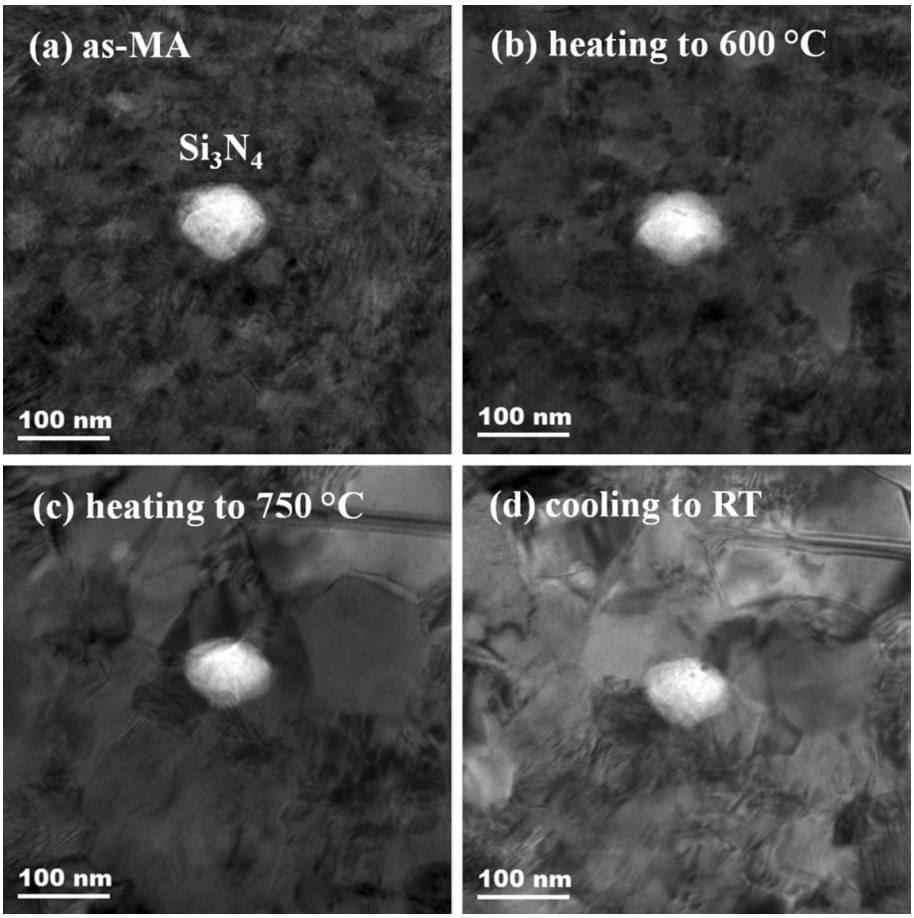

Fig. 3 Snapshots of MA powders with addition of Si_3N_4 during heating and cooling: **a** as-MA powders, **b** heating to 600 °C, **c** heating to 750 °C, **d** cooling to RT

Si_3N_4 particle appeared unchanged during heating to 750 °C as well as subsequent cooling.

Figure 4 shows microstructural evolution of the MA powders with addition of Er_2O_3 during heating and cooling. As shown in Fig. 4a, no particles were observed in the as-MA powders. The different contrasts were resulted from different local strains introduced during the MA process. Recrystallization seemed to begin at around 770 °C (Fig. 4b), which was higher than that of the MA powders with addition of Si_3N_4 (Fig. 3). The specimen was further heated to 950 °C (Fig. 4c), and then cooled to RT (Fig. 4f). The grains appeared to grow during both heating and subsequent cooling. Interestingly, precipitates with different sizes appeared after grain growth, as shown in Fig. 4d. The particles indicated by circles had relatively large sizes of around 20 nm, while the particles indicated by arrows were approximately 5 nm. More fine particles precipitated from the matrix during continuous cooling, as indicated by the arrows in Fig. 4e. Both precipitates were identified as $Er_2Ti_2O_7$ based on HR image analyses (Fig. 5a, b). Figure 5c shows the size distribution of $Er_2Ti_2O_7$ particles, and their average size was approximately 10 nm.

The in situ TEM results demonstrate that the precipitation of $Er_2Ti_2O_7$ particles was closely related to strain recovery and grain growth. Heavy deformation during the MA process introduced a variety of crystal defects, such as dislocations, vacancies and increased grain boundaries, which can be manifested by the large strain and ultrafine crystallite size in the as-MA powders (Fig. 1). These crystal defects could extend the solubility of solute atoms in the matrix [4]. However, they were annihilated with increasing temperature, which was confirmed by the strain recovery shown in Fig. 1b. During further heating to 950 °C and subsequent cooling, grain coarsening occurred after recrystallization, and thereby the grain boundary area decreased. Both the annihilation of defects and decreased grain boundaries would reduce the solubility of solute atoms in the matrix, consequently resulting in the precipitation of nanoparticles. According to the XRD results, approximately 66% of the strain was relieved by 800 °C. Therefore, it is reasonable to assume that some precipitates would have developed at relatively low temperatures due to the relief of strain. These early precipitated nanoparticles would grow to a relatively large size, while those that precipitated later would be relatively fine. This is consistent with the two sizes of precipitates indicated respectively by the circles and arrows in Fig. 4d, e. The in situ TEM

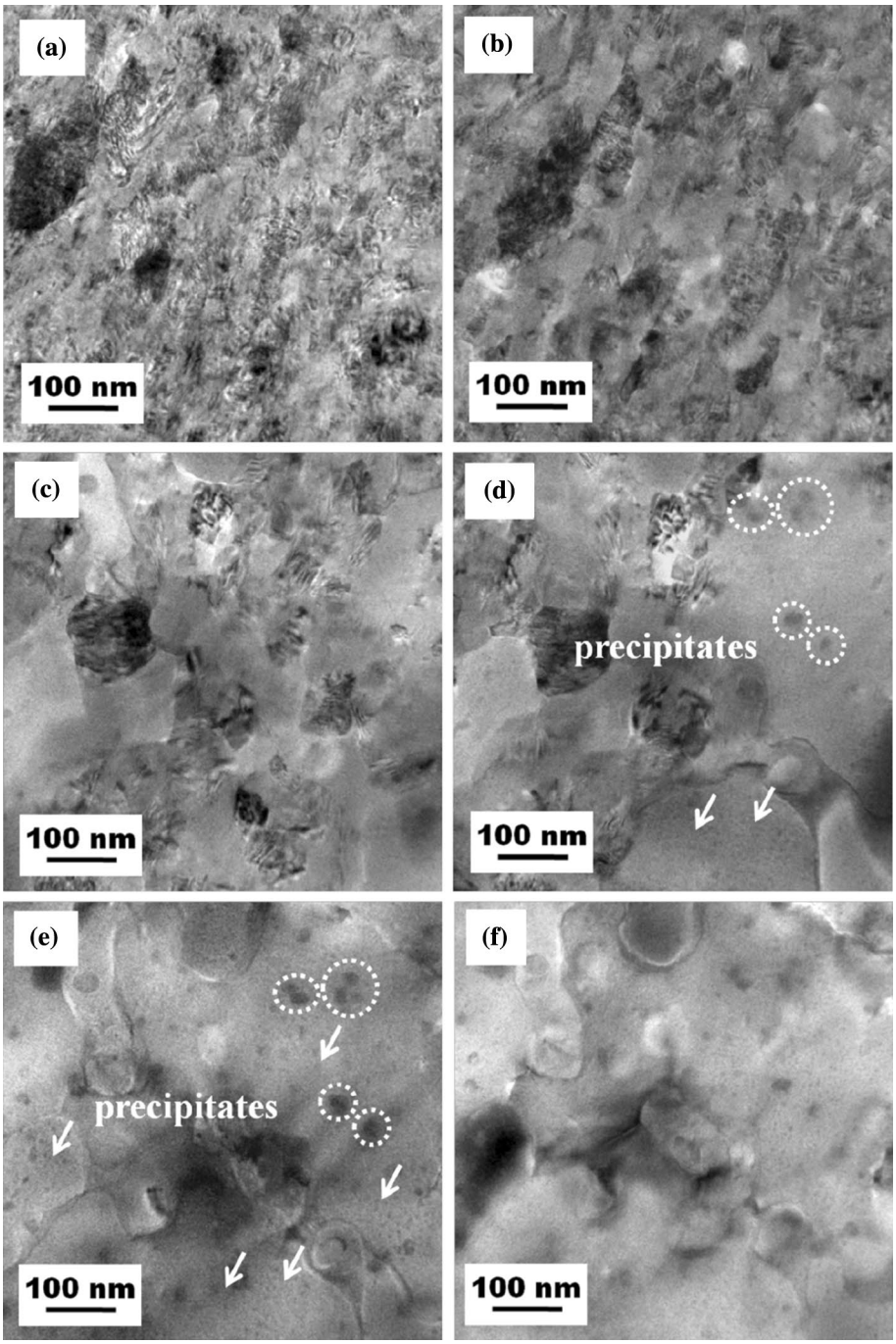

Fig. 4 Snapshots of MA powders with addition of Er_2O_3 during heating and cooling: **a** as-MA powders, **b** heating to 770 °C, **c** heating to 950 °C, **d** cooling to 937 °C, **e** cooling to 800 °C, **f** cooling to RT

observation results provide direct evidence for the precipitation mechanism in nickel-based MA powders.

In comparison to the MA powders with addition of Si_3N_4, the MA powders with addition of Er_2O_3 exhibited slower recovery of strain, higher recrystallization temperature, and greater grain coarsening resistance. This is attributed to the fact that the Si_3N_4 particles were not dissolved into the matrix; the non-dissolved large Si_3N_4 particles had a negligible effect in stabilizing the microstructure. However, the Er_2O_3 particles were dissolved into the matrix during MA process. The solute atoms precipitated during heating in the form of $Er_2Ti_2O_7$, with a finer size of approximately 10 nm. These fine nanoparticles were effective in retarding recrystallization and grain coarsening, which has been demonstrated in other ODS alloys [17, 18].

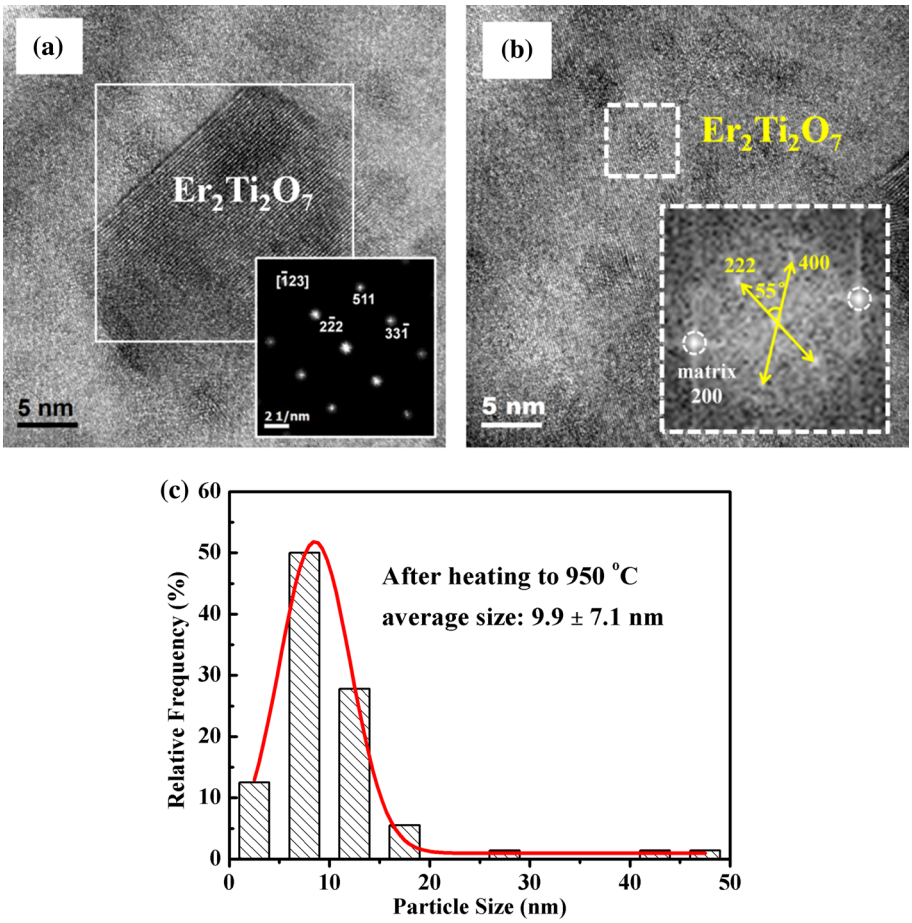

Fig. 5 TEM results of precipitates in MA powders with addition of Er_2O_3 after heating to 950 °C: **a** HR image of relatively large precipitate with the FFT image inset, **b** HR image of fine precipitate with the FFT image inset, **c** size distribution

4 Conclusions

The microstructural evolution of oxide and nitride dispersed nickel-based MA powders was investigated using high-temperature XRD and in situ TEM. The following conclusions can be drawn:

1. The MA powders with addition of Si_3N_4 particles exhibited faster strain recovery and grain coarsening, as the added Si_3N_4 particles were not dissolved into the matrix during MA process.
2. The added Er_2O_3 particles were dissolved during MA process, and precipitation of $Er_2Ti_2O_7$ with an average size of 10 nm was confirmed by in situ TEM, giving slower strain recovery and greater grain coarsening resistance.
3. The precipitation of nanosized $Er_2Ti_2O_7$ was related to strain recovery and grain growth, as they reduced the solubility of solute atoms in the matrix, consequently resulting in the precipitation.

Acknowledgements This study was granted by the R&D Program of Korea Atomic Energy Research Institute (KAERI). H.N. Han was supported by the National Research Foundation of Korea (NRF) granted by the Korea government (MSIT) (No. NRF-2015R1A5A1037627).

References

1. K. Murty, I. Charit, J. Nucl. Mater. **383**, 189–195 (2008)
2. S.J. Zinkle, G. Was, Acta Mater. **61**, 735–758 (2013)
3. S. Ukai, M. Fujiwara, J. Nucl. Mater. **307**, 749–757 (2002)
4. C. Suryanarayana, Prog. Mater. Sci. **46**, 1–184 (2001)
5. T. Okuda, M. Fujiwara, J. Mater. Sci. Lett. **14**, 1600–1603 (1995)
6. M. Alinger, G. Odette, D. Hoelzer, Acta Mater. **57**, 392–406 (2009)
7. H. Zhang, M.J. Gorley, K.B. Chong, M.E. Fitzpatrick, S.G. Roberts, P.S. Grant, J. Alloys Compd. **582**, 769–773 (2014)
8. M. Brocq, B. Radiguet, S. Poissonnet, F. Cuvilly, P. Pareige, F. Legendre, J. Nucl. Mater. **409**, 80–85 (2011)
9. M. Laurent-Brocq, F. Legendre, M.-H. Mathon, A. Mascaro, S. Poissonnet, B. Radiguet, P. Pareige, M. Loyer, O. Leseigneur, Acta Mater. **60**, 7150–7159 (2012)
10. H. Kishimoto, M.J. Alinger, G.R. Odette, T. Yamamoto, J. Nucl. Mater. **329**, 369–371 (2004)

11. P. He, P. Gao, Q. Tian, J. Lv, W. Yao, Mater. Lett. **209**, 535–538 (2017)
12. M. Ratti, D. Leuvrey, M. Mathon, Y. De Carlan, J. Nucl. Mater. **386**, 540–543 (2009)
13. G. Zhang, Z. Zhou, K. Mo, Y. Miao, S. Li, X. Liu, M. Wang, J.-S. Park, J. Almer, J.F. Stubbins, Mater. Des. **98**, 61–67 (2016)
14. J. Rodríguez-Carvajal, Laboratoire Léon Brillouin (CEA-CNRS), CEA/Saclay 91191 (2003)
15. H. Rietveld, J. Appl. Crystallogr. **2**, 65–71 (1969)
16. Y. Kimura, H. Hidaka, S. Takaki, Mater. Trans. JIM **40**, 1149–1157 (1999)
17. M. Miller, D. Hoelzer, E. Kenik, K. Russell, Intermetallics **13**, 387–392 (2005)
18. X. Mao, K.H. Oh, J. Jang, Mater. Charact. **117**, 91–98 (2016)